Transport properties in monolayer–bilayer–monolayer graphene planar junctions*

Kai-Long Chu(储开龙)[1], Zi-Bo Wang(王孜博)[2], Jiao-Jiao Zhou(周娇娇)[1], and Hua Jiang(江华)[1,†]

[1] College of Physics, Optoelectronics and Energy Soochow University, Suzhou 215006, China
[2] Microsystems and Terahertz Research Center, China Academy of Engineering Physics, Chengdu 610200, China

(Received 24 February 2017; revised manuscript received 13 April 2017; published online 10 May 2017)

The transport study of graphene based junctions has become one of the focuses in graphene research. There are two stacking configurations for monolayer–bilayer–monolayer graphene planar junctions. One is the two monolayer graphene contacting the same side of the bilayer graphene, and the other is the two-monolayer graphene contacting the different layers of the bilayer graphene. In this paper, according to the Landauer–Büttiker formula, we study the transport properties of these two configurations. The influences of the local gate potential in each part, the bias potential in bilayer graphene, the disorder and external magnetic field on conductance are obtained. We find the conductances of the two configurations can be manipulated by all of these effects. Especially, one can distinguish the two stacking configurations by introducing the bias potential into the bilayer graphene. The strong disorder and the external magnetic field will make the two stacking configurations indistinguishable in the transport experiment.

Keywords: monolayer graphene, bilayer graphene, graphene planar junction

PACS: 72.80.Vp, 72.25.–b, 73.22.Pr, 81.05.ue **DOI:** 10.1088/1674-1056/26/6/067202

1. Introduction

Graphene, a flake of carbon with honeycomb structure and atomic thickness, has been known for its excellent characteristics in mechanical, electrical, optical, thermal, etc, since it was fabricated in the laboratory in 2004.[1–4] For the monolayer graphene, the energy band is gapless. Thus, it possesses the characters of massless Dirac fermions,[5] such as Klein tunneling,[6] quasi-bound states,[7] Veselago lensing,[8] high mobility,[9] etc. The tailoring and the stacking of the graphene can make up more interesting systems, e.g., nanoribbon and multilayers graphene.[10,11] The shortcoming of the monolayer graphene structure is the difficulty in opening an adequate gap, which greatly restricts its practical application. Fortunately, such a problem can be overcome in bilayer graphene systems by applying the bias potential between the different layers.[12–17] Nowadays, plenty of quantum electronic devices fabricated with monolayer or bilayer graphene are extensively studied due to their excellent physical properties.[18–45]

The hybrid graphene structures, which contain both monolayer and bilayer graphene in one sample, have aroused great interest recently.[29–34,44–50] The hybrid structures inherit the advantages of the two types of graphene, and may have promising applications in devices. In theory, the simplest hybrid graphene structure is the monolayer–bilayer graphene junction. Although there are lots of theoretic proposals focusing on the exotic properties recently,[30–33,44–49] the experimental studies of monolayer–bilayer graphene junctions are very few.[34,50] The difficulty originates from the growing process. In order to fabricate a monolayer–bilayer graphene junction, one needs to grow a large bilayer graphene area that contact the monolayer graphene. However, in real experiment, it is common to observe a small bilayer island surrounded by monolayer (e.g, see Fig. 1 in Ref. [4]). That is to say, it is much easier to fabricate a device with the monolayer–bilayer–monolayer structure in experiment. Nevertheless, there are still few studies on monolayer–bilayer–monolayer planar junction at present. Interestingly, there are two stacking configurations for such a type of junction. One is named bottom-bottom configuration, where the two monolayer graphene leads contact the bottom layer of the bilayer graphene region (see Fig. 1(a)). The other is called bottom–up configuration, where two monolayer graphene leads contact the different layers of the bilayer graphene (see Fig. 1(b)). It is natural to ask what exotic properties a monolayer–bilayer–monolayer planar junction possesses and how we can distinguish its two stacking configuration in experiment.

In this paper, we explore the transport properties of monolayer–bilayer–monolayer graphene planar junctions under both bottom-bottom configuration and bottom–up configuration. With the help of tight-binding model and Landauer–Büttiker formula, we obtain the conductance of the system with both disorder and magnetic field by changing the Fermi energy, the gate potential in the left/central/right part and the bias potential in the bilayer graphene. We find that the con-

*Project supported by the National Natural Science Foundation of China (Grant No. 11374219), the Jiangsu Provincial Natural Science Foundation, China (Grant No. BK20160007), and the Research Fund for the Doctoral Program of Higher Education of China.

†Corresponding author. E-mail: jianghuaphy@suda.edu.cn

© 2017 Chinese Physical Society and IOP Publishing Ltd

ductance of the system can be manipulated by Fermi energy, gate potential and bias potential and so on. In particular, under finite bias potential U, the conductance behaviors in bottom–bottom configuration are much different from those in bottom–top configuration. Based on such a transport phenomenon, an efficient way that these two configurations can be distinguished is proposed. The conductance of the system decreases rapidly in the presence of the disorder, and shows unique plateau features under the external magnetic field. Both disorder and external magnetic field can eliminate the distinction of conductance between the bottom–bottom and bottom–top configuration, making these two configurations indistinguishable.

The rest of this paper is organized as follows. In Section 2, we introduce the two studied stacking structures. Besides, the tight-binding models and the numerical methods are described. Subsection 3.1 is dedicated to the influences of disorder, gate potential and the bias potential. Subsection 3.2 focuses on the effect of the magnetic field. Finally, Section 4 is for summarizing our main results.

2. Models and methods

In this paper, as shown in Figs. 1(a) and 1(b), we take into consideration two stacking configurations with monolayer–bilayer–monolayer graphene planar junctions. The red (black) refers to the layer on the top (bottom). Each junction can be divided into three parts: two semi-infinite monolayer graphene leads and a finite size bilayer graphene central region. In experiment, the magnetic field and the electric field are the two important tools to manipulate the transport properties of the systems. In order to be consistent with experimental condition, we assume that the magnetic field is uniformly distributed in the global region while the electric field in each region can be tuned independently. In the tight-binding representation, the Hamiltonian can be written as

$$\begin{aligned} H &= H_{\rm L} + H_{\rm C} + H_{\rm R} + H_{\rm LC} + H_{\rm RC}, \\ H_{\rm L/R} &= \sum_{\langle i,j\rangle} t\, {\rm e}^{{\rm i}\phi_{ij}} c_i^{\dagger} c_j + {\rm h.c.} + \sum_i V_{\rm L/R} c_i^{\dagger} c_i, \\ H_{\rm C} &= \sum_{\langle i,j\rangle} t\, {\rm e}^{{\rm i}\phi_{ij}} c_i^{\dagger} c_j + \sum_{\langle i,j\rangle} t_1 c_i^{\dagger} c_j + {\rm h.c.} \\ &\quad + \sum_i (V_{\rm C} + U_i + \omega_i) c_i^{\dagger} c_i, \\ H_{\rm LC/RC} &= \sum_{\langle i,j\rangle} t\, {\rm e}^{{\rm i}\phi_{ij}} c_i^{\dagger} c_j + {\rm h.c.}, \end{aligned} \tag{1}$$

where $H_{\rm L}$ ($H_{\rm R}$) and $H_{\rm C}$ describe the Hamiltonians of the left (right) leads and the central region; $H_{\rm LC}$ ($H_{\rm RC}$) is the coupling term between the left (right) lead and the central region; subscript $\langle i,j\rangle$ refers to a pair of the nearest neighbor sites, $c_i^{\dagger}$ (c_j) denotes the creation (annihilation) operator on site i (j), t and t_1 are the nearest neighbor hopping integrals for intra

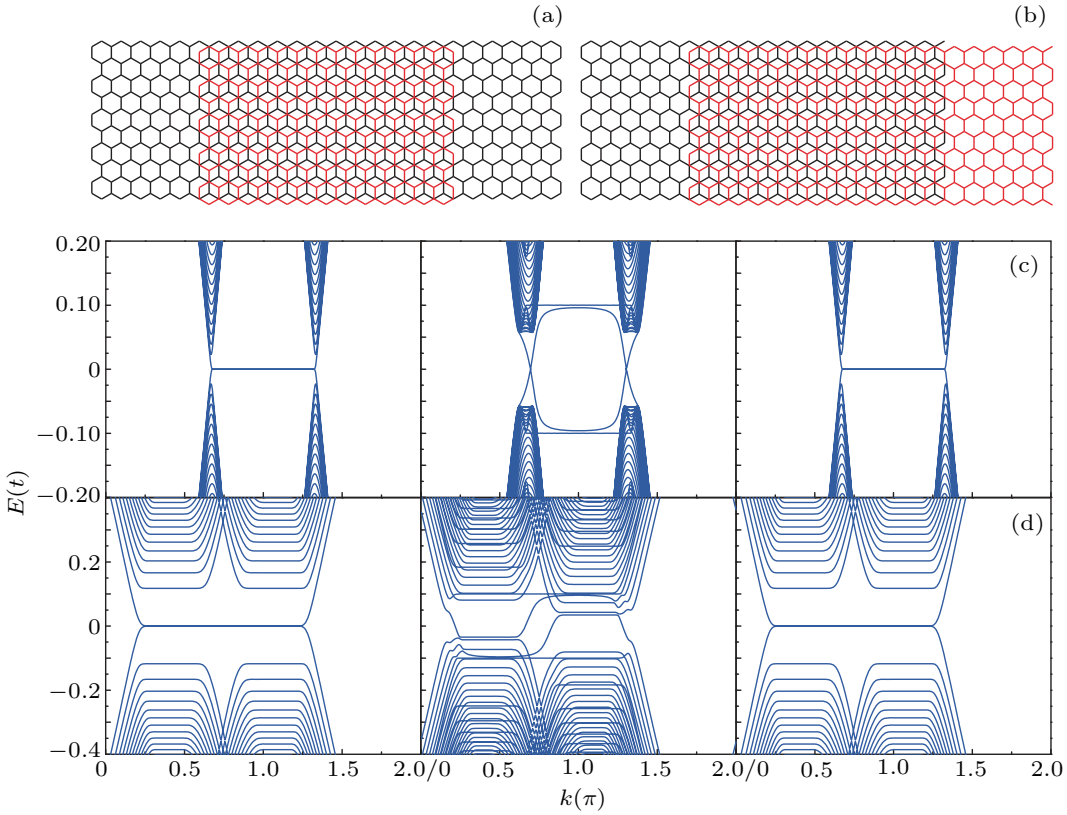


Fig. 1. (color online) ((a) and (b)) Schematics of monolayer–bilayer–monolayer graphene in two different stacking structures, respectively. The ribbon junction can be separated into three parts: the left/right monolayer graphene leads and the central part. The disorder only appear in the central bilayer graphene region with size $L \times N$. In panels (a) and (b), $N = 5$ and $L = 13$. Panels (c) and (d) show the energy bands of the three parts with and without the magnetic field. The parameters are set to be $N = 80$, $t_1 = 0.14t$, $U = 0.1t$, $B = 0$ (c), and $B = 100$ T (d).

and inter layers, ϕ_{ij} is the extra phase induced by the external perpendicular magnetic field and expressed as $\phi_{ij} = \frac{\hbar}{e}\int_i^j A\,\mathrm{d}r$ with $A = (-By, 0, 0)$ being the vector potential; V_i=$V_{\mathrm{L/C/R}}$ is the gate potential in the left/central/right part. The perpendicular electric field can also introduce a bias potential with U_i=$U/-U$ in the top/bottom layer of bilayer graphene. The disorder is described by on-site energy ω_i that is uniformly distributed in the range $[-W, W]$, with W denoting the disorder strength.

As shown in Figs. 1(c) and 1(d), the band structures of the corresponding monolayer/bilayer/monolayer graphene parts with and without the magnetic field are plotted, respectively. For convenience, we have set $V_\mathrm{L} = V_\mathrm{C} = V_\mathrm{R} = 0$, because the presence of V_i just globally shifts the energy spectrum. Without the magnetic field, all three parts form standard monolayer/bilayer graphene ribbon band structure. The potential U opens a band gap $2U$ in the central part. If the magnetic field is added, the band forms the Landau levels both on the monolayer and bilayer condition. Interestingly, the 0th Landau levels in K/K' are absent in conduction/valence bands in bilayer graphene.

With the help of Landauer–Büttiker formula, the linear conductance at zero temperature of the studied systems can be calculated from $G_\mathrm{LR} = (2\mathrm{e}^2/h)T_\mathrm{LR}(E_\mathrm{F})$, where $T_\mathrm{LR}(\varepsilon) = \mathrm{Tr}[\Gamma_\mathrm{L}G^\mathrm{r}\Gamma_\mathrm{R}G^\mathrm{a}]$ is the transmission coefficient, $G^\mathrm{r} = [G^\mathrm{a}]^+ = [E_\mathrm{F} - H_\mathrm{C} - \Sigma_\mathrm{L} - \Sigma_\mathrm{R}]^{-1}$ being the Green function of the central region; $\Gamma_{\mathrm{L/R}}$ is the linewidth function and expressed as $\Gamma_\mathrm{LR} = \mathrm{i}[\Sigma^\mathrm{r}_\mathrm{LR} - \Sigma^\mathrm{a}_\mathrm{LR}]$ being the retard self-energy that couples to the lead-α, which can be directly calculated.[51–56] The band structure plotted in Fig. 1 will help us understand the conductance of the system better. During the following numerical calculation, we have set the energy t to be a unit and $t_1 = 0.14t$. The central region size is fixed to be $N = 80$ and $L = 100$. G_LR is averaged over 500 disorder configurations.

3. Results and discussion

3.1. Numerical results without magnetic field

Figure 2 shows the plots of the conductance G_LR versus E_F for different disorder strengths. Obviously, both configurations have the same G_LR at Fermi energy E_F and $-E_\mathrm{F}$. This means that the type of the carriers will not influence the conductance. Due to the redundant scattering from mismatched interface of monolayer–bilayer graphene, G_LR does not show the regular plateaus even in the absence of disorder (see black line in Fig. 2). By shifting the Fermi energy E_F away from the charge neutral point, more incident modes will be involved in the transport processes (see Fig. 1(c)). Therefore, G_LR increases being accompanied with only small oscillations. When disorder is considered, the induced scattering will suppress the conductance G_LR. As shown in Figs. 2(a) and 2(b), G_LR decreases rapidly by increasing the disorder strength W. Interestingly, the average of the disorder configuration smoothens the variation of the conductance G_LR. Comparing with the $W = 0$ case, the oscillation of G_LR at large W becomes negligible.

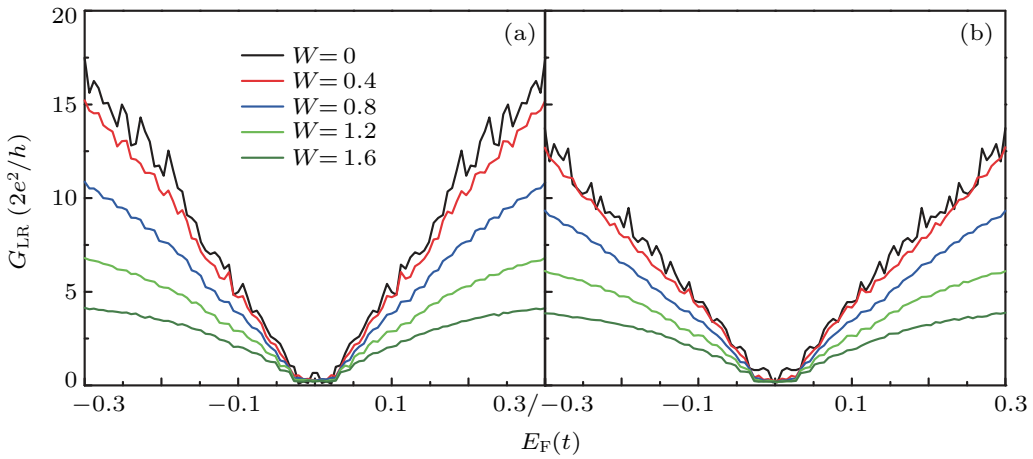


Fig. 2. (color online) Plots of conductance G_LR versus Fermi energy E_F for different values of disorder strength $W = 0.0$, 0.4, 0.8, 1.2 1.6. Panels (a) and (b) correspond to the bottom–bottom and bottom–top configurations respectively. The other parameters are $V_\mathrm{L} = V_\mathrm{C} = V_\mathrm{R} = 0$, and $U = 0$.

By comparing the bottom–bottom configuration and bottom–up configuration cases, G_LR shows two major different behaviors. Firstly, in the absence of disorder and E_F is located around the charge neutral point, G_LR shows a peak (dip) with value $2e^2/h(0)$ in the former (later) case, which may be attributed to the difference in situation for the mismatch of wavefunction parities.[35] Secondly, G_LR is always lager in bottom–bottom configuration than that in bottom–up configuration. Because, in the transport processes, in the former case the carriers pass through the same layer while in the latter case the carriers need jump from bottom layer to top layer.

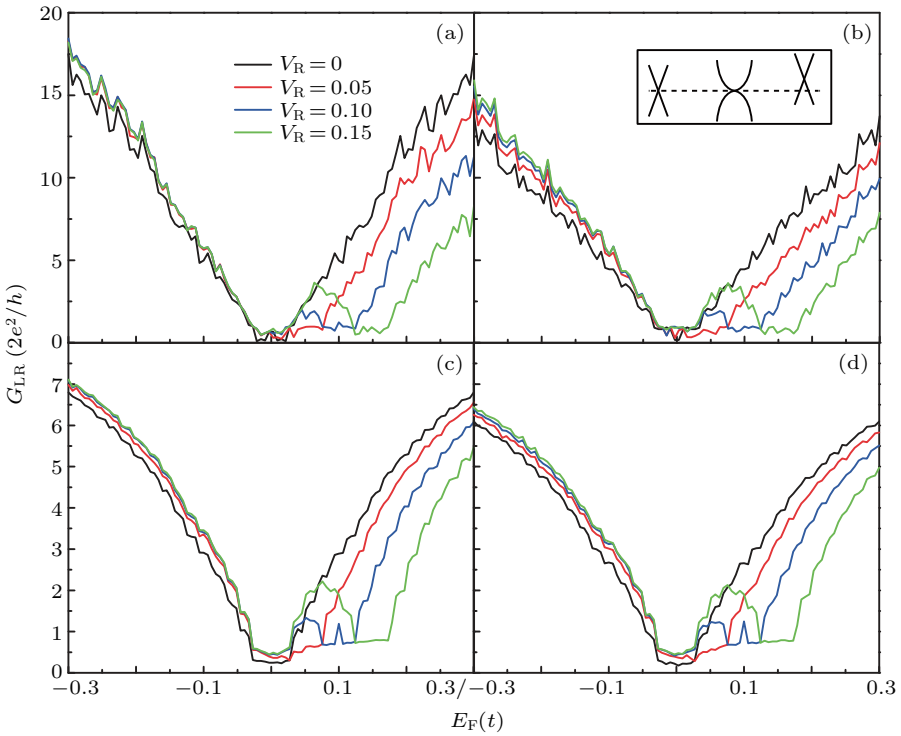


Fig. 3. (color online) Plots of conductance G_{LR} versus E_F under different gate potentials in the right lead $V_R = 0.00, 0.05, 0.10, 0.15$. Panels (a) and (c) correspond to the bottom–bottom configuration with the values of disorder strength $W = 0$ and $W = 1.2$, respectively. Panels (b) and (d) correspond to the bottom–top configuration with $W = 0$ and $W = 1.2$. The other parameters are $V_L = V_C = 0$, and $U = 0$. The inset shows the corresponding band structures in the three parts.

Next, we investigate how G_{LR} is influenced by potential on the right lead V_R. The main results are plotted in Fig. 3. In general, plots of G_{LR} versus Fermi energy E_F and disorder strength W hold the majority of behaviors described in Fig. 2. However, a big difference emerges when E_F is located inside the interval $[0,V_R]$. The G_{LR} increases initially until Fermi energy reaches $E_F = V_R/2$ and then decreases until $E_F = V_R$. Such a behavior originates from the fact that G_{LR} is controlled by the minimal conduction modes in the three parts of the configuration. When $E_F < V_R/2$, G_{LR} is determined by the number of conduction modes in the left monolayer or bilayer graphene, which increases with E_F. On the contrary, when $V_R/2 < E_F < V_R$, G_{LR} is determined by the number of conduction modes in the right monolayer, which decreases with E_F.

Figure 4 shows the plots of the conductance G_{LR} versus Fermi energy E_F for different values of U. The presence of U opens a gap $2U$, where G_{LR} equals zero. Significantly, in the absence of disorder, one can find that G_{LR} shows totally opposite behaviors between the bottom–bottom configuration and bottom–top configuration. First, in the former configuration, the particle–hole symmetry of the whole systems is broken, where $G_{LR}(E_F)$ is no longer equal to $G_{LR}(-E_F)$. In the latter configuration, since $G_{LR}(E_F) = G_{LR}(-E_F)$, the particle–hole symmetry still holds. Second, in the former configuration, the presence of U enhances G_{LR} in the valence band while greatly suppresses G_{LR} in the conduction band. On the contrary, by increasing U, G_{LR} is suppressed heavily in both conduction and valence bands in the latter configuration. In experiment, the different behaviors of G_{LR} with bias U can be used to distinguish the two configurations.

The unique properties of G_{LR} under U can be briefly explained, following Ref. [36]. In low energy regime, the wavefunction of bulk state in bilayer graphene is expressed as spinor $[\varphi_B, \varphi_T]^T$, where $\varphi_B(\varphi_T)$ represents the amplitude in the bottom (top) layer. The presence of U breaks the equal amplitudes of the wavefunction ($|\varphi_B| = |\varphi_T|$), and leads to the redistribution of the carriers in the bilayer graphene.[36] For $U > 0$, $|\varphi_B| > |\varphi_T|$ ($|\varphi_B| < |\varphi_T|$) and the ratio $|\varphi_B/\varphi_T|$ increases (decreases) with U increasing when Fermi energy E_F is in valence (conduction) band. For the bottom–bottom configuration, G_{LR} is proportional to $|\varphi_B|^2$. Thus, the breaking of the particle–hole symmetry and the more conductive properties in valence band can be observed in Fig. 4(a). Oppositely, for the bottom–top configuration, G_{LR} is proportional to $|\varphi_B\varphi_T|$. The preserve of particle–hole symmetry and the dependence of G_{LR} on U that are plotted in Fig. 4(b) can be understood.

Next, we study the effects of central region gate potential V_C on G_{LR} under various values of bias potential U. As shown in Fig. 5, the main features observed in Fig. 4 still hold. The only obvious exception is that there is an additional gap (dip) in the region around $E_F = V_C$ with (without) finite U. Such a phenomenon means that for any E_F, the transport properties of the system can be greatly manipulated by the local gate in the central region.

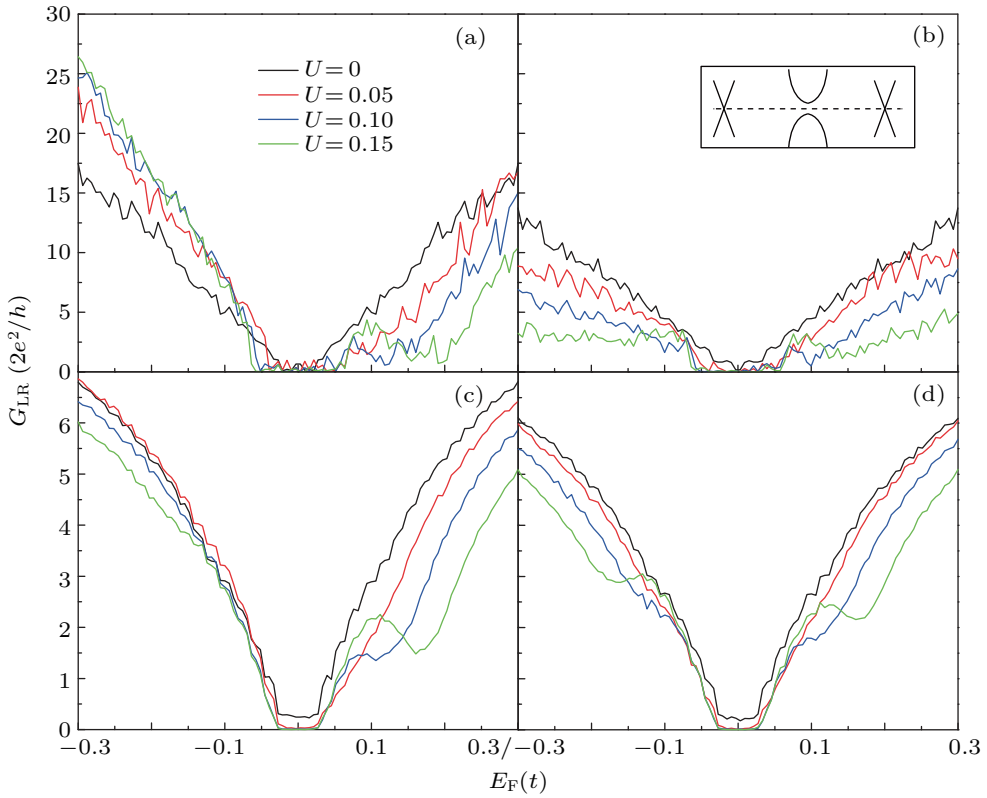


Fig. 4. (color online) Plots of conductance $G_{\rm LR}$ versus Fermi energy $E_{\rm F}$ for different values of bias potential $U = 0.00$, 0.05, 0.10, 0.15. Panels (a) and (c) correspond to the bottom–bottom configuration with the values of disorder strength $W = 0$ and $W = 1.2$. Panels (b) and (d) correspond to the bottom–top configuration under $W = 0$ and $W = 1.2$. The other parameters are $V_{\rm L} = V_{\rm C} = V_{\rm R} = 0$. The inset shows the corresponding band structures in the three parts.

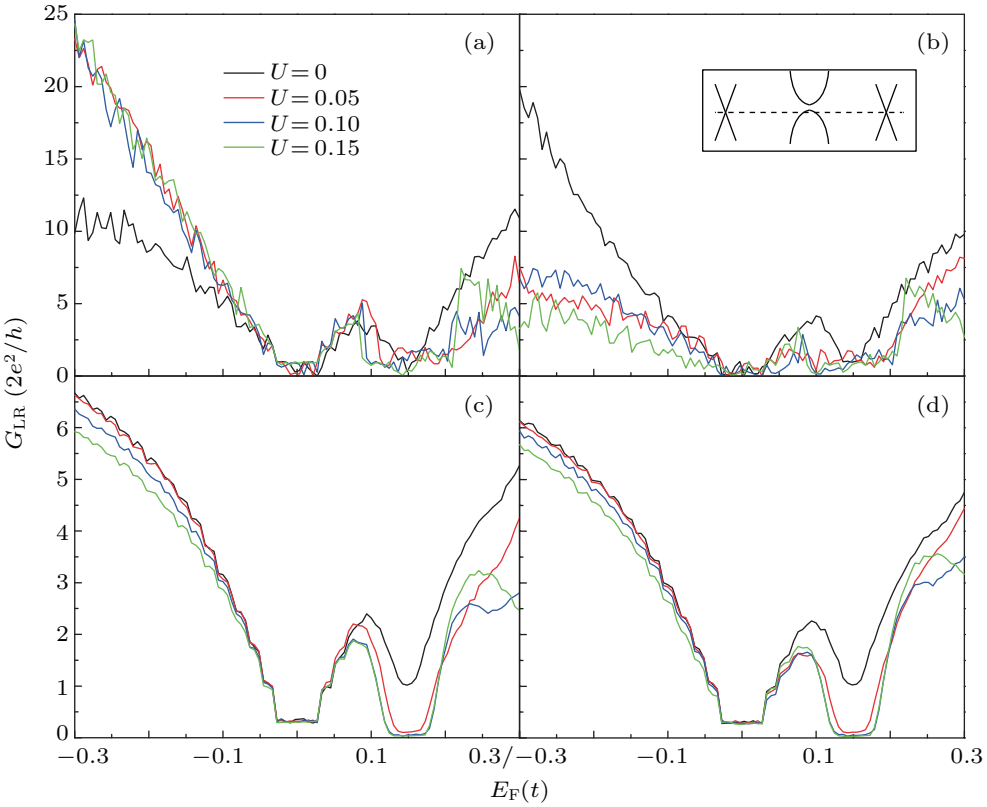


Fig. 5. (color online) Plots of conductance $G_{\rm LR}$ versus Fermi energy $E_{\rm F}$ for different values of bias potential $U = 0.00$, 0.05, 0.10, 0.15. Panels (a) and (c) correspond to the bottom–bottom configuration with the values of disorder strength $W = 0$ and $W = 1.2$. Panels (b) and (d) correspond to the bottom–top configuration under $W = 0$ and $W = 1.2$. The other parameters are $V_{\rm L} = V_{\rm R} = 0$, and $V_{\rm C} = 0.15$. The inset shows the corresponding band structures in the three parts.

In addition, in Figs. 3(c) and 3(d), 4(c) and 4(d), and 5(c) and 5(d), the effects of disorder on $G_{\rm LR}$ are carefully examined. Generally speaking, the disorder does not only reduce the conductance, but also smoothens the abrupt variation of $G_{\rm LR}$. For example, comparing with Figs. 5(a) and 5(b), the absence of oscillations makes the variation tendencies of $G_{\rm LR}$ in Figs. 5(c) and 5(d) become much clear. Importantly, one can find that the strong disorder eliminates the distinction of $G_{\rm LR}$ between the two stacking configurations. Though big difference emerges between Fig. 4(a) (Fig. 5(a)) and Fig. 4(b) (Fig. 5(b)), the strong disorder makes Fig. 4(c) (Fig. 5(c)) and Fig. 4(d) (Fig. 5(d)) indistinguishable.

In principle, the different transport behaviors can be used to experimentally distinguish the bottom–bottom configuration and bottom–up configuration. Figures 4 and 5 show that the local gate induced bias potential U can introduce the different behaviors of $G_{\rm LR}$ with $E_{\rm F}$ increasing. However, locating a gate in the small central region needs precise technique, which is not economic in such a type of experiment. It is much easier to use a global gate. In this case, the point is whether we can still distinguish these two configurations.

Under the global gate, the total potentials in the same layers should be equal. That is to say, for the bottom–bottom configuration case, the potential in the right lead equals the potential in the bottom layer of bilayer graphene ($V_{\rm R} = V_{\rm L} = 0$). On the contrary, for the bottom–top configuration, the potential in the right lead equals that in the top layer of bilayer graphene ($V_{\rm R} = 2U$, $V_{\rm L} = 0$). Figure 6 shows the plots of conductance $G_{\rm LR}$ versus $E_{\rm F}$ under various potentials. Though $G_{\rm LR}$ shows some different behaviors (e.g., the charge netural points are shifted toward energy U), the important features of distinguishing these two configurations are still hold. Like Figs. 4(a) and 4(b) and Figs. 5(a) and 5(b), the different behaviors of $G_{\rm LR}$ with U and $E_{\rm F}$ in both conduction and valence band between the two configurations can be clearly observed in Figs. 6(a) and 6(b). In conclusion, one can also use a simple global gate to distinguish the configurations.

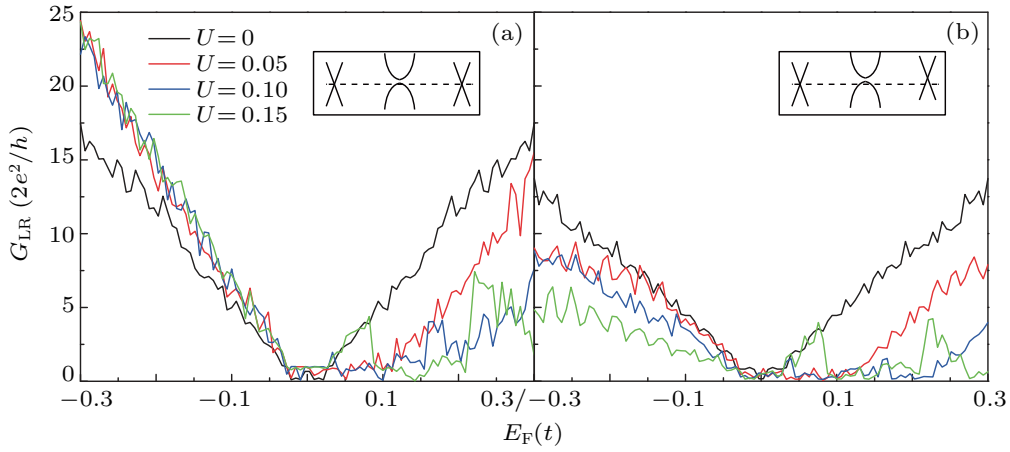


Fig. 6. (color online) Plots of conductance $G_{\rm LR}$ versus Fermi energy $E_{\rm F}$ for the values of bias potential $U = 0.00, 0.05, 0.10, 0.15$. The disorder strength $W = 0$. Panel (a) corresponds to the bottom–bottom configuration with $V_{\rm L} = V_{\rm R} = 0$, $V_{\rm C} = U$. Panel (b) corresponds to the bottom–top configuration with $V_{\rm L} = 0$, $V_{\rm C} = U$, $V_{\rm R} = 2U$. The inset shows the corresponding band structures in the three parts.

3.2. Results in the presence of magnetic field

In this subsection, we study how the magnetic field influences the transport properties of the system. Unlike the scenario in the above subsection, under strong magnetic field, the bulk states in both monolayer and bilayer graphene form the Landau levels. The transport processes in the system are dominant by the corresponding edge states. Therefore, $G_{\rm LR}$ shows totally opposite behaviors to the situations with no magnetic field. Under strong magnetic field and finite disorder, $G_{\rm LR}$ is not sensitive to the stacking configuration. We have checked many cases, the behaviors of $G_{\rm LR}$ are nearly the same for the configurations bottom–bottom and bottom–up. In the following, we only describe the variations of $G_{\rm LR}$ under different conditions without comparing the two configurations.

Figure 7 shows the plots of $G_{\rm LR}$ versus $E_{\rm F}$ for different disorder strengths, with magnetic field B fixed at 100 T ($B = 100$ T). A series of plateaus originating from the corresponding Landau levels emerge in $G_{\rm LR}$.[57–59] With the increase of disorder strength, the plateaus tend to disappear. For example, there is no plateau for $W > 3.0$ in Fig. 7(a) nor Fig. 7(b). Moreover, for $E_{\rm F} < 0$, the plateau becomes unclear when both monolayer and bilayer graphene are in high Landau level states. For $E_{\rm F}$ in the valence band, there are no obvious plateaus in neither of configurations. In addition, if all three parts of system are in the hole-type low Landau level states, a stable plateau always exists even when the disorder strength W is strong (e.g., $E_{\rm F} \in [-0.1, 0.1]$ in Figs. 7(a) and 7(b)).

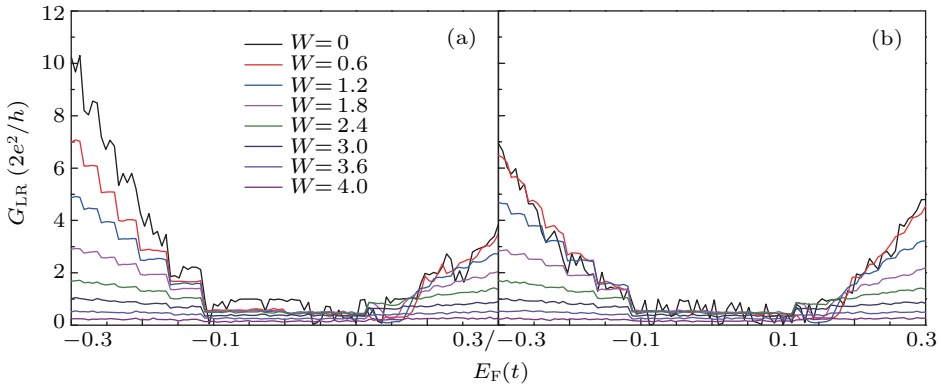


Fig. 7. (color online) Plots of conductance $G_{\rm LR}$ versus Fermi energy $E_{\rm F}$ under the values of disorder strength $W = 0.0, 0.6, 1.2, 1.8, 2.4, 3.0, 3.6, 4.2$. Panels (a) and (b) correspond to the bottom–bottom and bottom–top configurations, respectively. The other parameters are $V_{\rm L} = V_{\rm R} = 0$, $V_{\rm C} = 0.15$, $U = 0.1$, and $B = 100$ T.

In Fig. 8, we investigate the effects of potential $V_{\rm R}$ on $G_{\rm LR}$ under strong magnetic field. The plateaus exist in the whole energy region $[-0.3, 0.3]$. When $E_{\rm F} < 0$, the gate potential in the right lead $V_{\rm R}$ has little influence on conductance $G_{\rm LR}$. But when $E_{\rm F} > 0$, the right shifts of all the plateaus by $V_{\rm R}$ can be clearly observed.

In Fig. 9, we examine the relations of $G_{\rm LR}$ with the bias potential U and gate potential $V_{\rm C}$ in the central region under strong magnetic field. The presence of $V_{\rm C}$ shifts the charge neutral point of bilayer graphene, which clearly separates the variation tendencies of $G_{\rm LR}$ in the figure by $E_{\rm F} = V_{\rm C}$ (see Figs. 9(a) and 9(b)). As plotted in Fig. 1(c), the edge states also exist inside the bulk gap of bilayer graphene. However, for large U, we observe $G_{\rm LR} = 0$ around $E_{\rm F} = V_{\rm C}$ in Figs. 9(a) and 9(b). Because such a type of edge state does not originate from the Landau level.[60] Thus, those edge states are not robust against the disorder. Moreover, when Fermi energy $E_{\rm F} < V_{\rm C}$, a series of stable plateaus exists in $G_{\rm LR}$ for all values of U. In contrast, there is no plateau in $G_{\rm LR}$ when $E_{\rm F} > V_{\rm C}$ for neither of configurations.

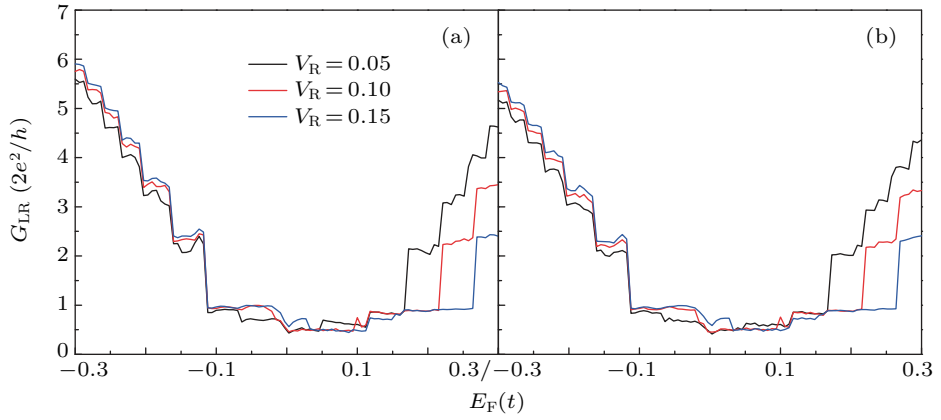


Fig. 8. (color online) Plots of conductance $G_{\rm LR}$ versus $E_{\rm F}$ under different gate voltages in the values of right lead $V_{\rm R} = 0.05, 0.10, 0.15$. Panels (a) and (b) correspond to the bottom–bottom and bottom–top configurations respectively. The other parameters are $V_{\rm L} = V_{\rm C} = U = 0$, $B = 100$ T, and $W = 1.2$.

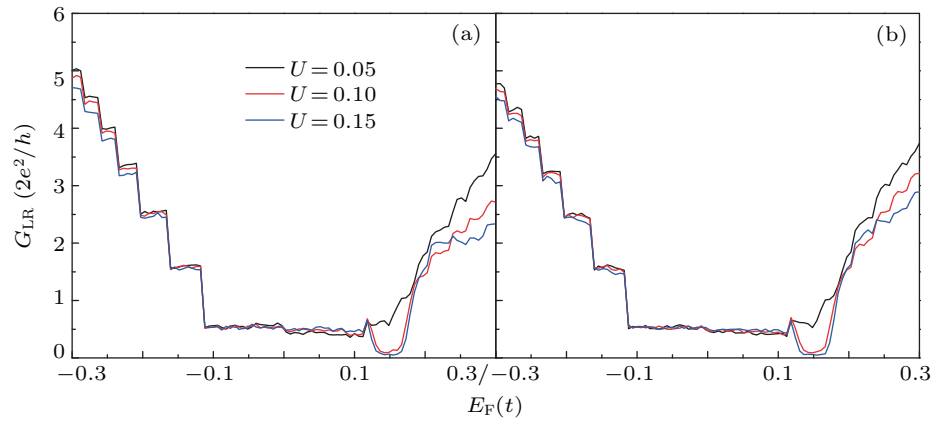


Fig. 9. (color online) Plots of conductance $G_{\rm LR}$ versus Fermi energy $E_{\rm F}$ for different values of bias potential $U = 0.05, 0.10, 0.15$. The gate potential in the central region is $V_{\rm C} = 0.15$. Panels (a) and (b) correspond to the bottom–bottom and bottom–top configurations, respectively. The other parameters are $V_{\rm L} = V_{\rm R} = 0$, $B = 100$ T, and $W = 1.2$.

Finally, although G_{LR} always exhibits the plateau features, we find that it is very difficult to obtain a quantized plateau value in monolayer–bilayer–monolayer graphene planar junction (see Figs. 7–9). Oppositely, under strong magnetic field and moderate disorder, the quantized plateaus only depend on the filling factor of the composed parts for G_{LR}, which have been reported in both monolayer–monolayer and monolayer–bilayer graphene planar junctions.[31–34,50,61,62] Such a difference may be attributed to much stronger scattering due to the mismatch interface and imperfect mixing of the edge states due to the small central region size in our studied system.

4. Summary

In this work, the electrical conductances of monolayer–bilayer–monolayer graphene planar junctions under both bottom–bottom configuration and bottom–up configuration are investigated. We find that the transport properties of the junctions can be controlled by the Fermi energy, the gate potential on each junction part, the bias potential on bilayer graphene, the disorder effect and the external magnetic field. Especially, according to the obvious difference between the transport behaviors of the different junctions under finite bias, we propose an efficient way that bottom–bottom configuration and bottom–up configuration can be distinguished in experiment.

Acknowledgment

We are grateful to S G Cheng and A M Guo for helpful discussions.

References

[1] Novoselov K S, Geim A K, Morozov S V, Jiang D, Zhang Y, Dubonos S V, Grigorieva I V and Firsov A A 2004 *Science* **306** 666
[2] Geim A K and Novoselov K S 2007 *Nat. Mater.* **6** 183
[3] Castro Neto A H, Guinea F, Peres N M R, Novoselov K S and Geim A K 2009 *Rev. Mod. Phys.* **81** 109
[4] Geim A K 2009 *Science* **324** 1530
[5] Novoselov K S, Geim A K, Morozov S V, Jiang D, Katsnelson M I, Grigorieva I V, Dubonos S V and Firsov A A 2005 *Nature* **438** 197
[6] Katsnelson M I, Novoselov K S and Geim A K 2006 *Nat. Phys.* **2** 620
[7] Silvestrov P G and Efetov K B 2007 *Phys. Rev. Lett.* **98** 016802
[8] Cheianov V V, Fal'ko V and Altshuler B L 2007 *Science* **315** 1252
[9] Morozov S V, Novoselov K S, Katsnelson M I, Schedin F, Elias D C, Jaszczak J A and Geim A K 2008 *Phys. Rev. Lett.* **100** 016602
[10] Li X, Wang X, Zhang L, Lee S and Dai H 2008 *Science* **319** 1229
[11] Malard L M, Pimenta M A A, Dresselhaus G and Dresselhaus M S 2009 *Phys. Rep.* **473** 51
[12] Castro E V, Novoselov K S, Morozov S V, Peres N M R, Lopes dos Santos J M B, Nilsson J, Guinea F, Geim A K and Castro Neto A H 2007 *Phys. Rev. Lett.* **99** 216802
[13] Samarakoon D K and Wang X Q 2010 *ACS Nano* **4** 4126
[14] Velasco J Jr, Jing L, Bao W, Lee Y, Kratz P, Aji V, Bockrath M, Lau C N, Varma C, Stillwell R, Smirnov D, Zhang F, Jung J and MacDonald A H 2012 *Nat. Nanotech.* **7** 156
[15] Zhang Y B, Tang T T, Girit C, Hao Z, Martin M C, Zettl A, Crommie M F, Shen Y R and Wang F 2009 *Nature* **459** 820
[16] Min H K, Sahu B, Banerjee S K and MacDonald A H 2007 *Phys. Rev. B* **75** 155115
[17] Fiori G and Iannaccone G 2009 *IEEE Electron Dev. Lett.* **30** 261
[18] He Z Z, Yang K W, Yu C, Liu Q B, Wang J J, Song X B, Han T T, Feng Z H and Cai S J 2016 *Chin. Phys. Lett.* **33** 86801
[19] Chen D H, Yang M, Duan H J and Wang R Q 2015 *Acta Phys. Sin.* **64** 097201 (in Chinese)
[20] Rezania H and Azizi F 2016 *Chin. Phys. B* **25** 097303
[21] Jatiyanon K, Tang I M and Soodchomshom B 2016 *Chin. Phys. B* **25** 078104
[22] He Z Z, Yang K W, Yu C, Liu Q B, Wang J J, Li J, Lu W L, Feng Z H and Cai S J 2016 *Chin. Phys. B* **25** 067206
[23] Lee J K, Lee S C, Ahn J P, Kim S C, Wilson J I B and John P 2008 *J. Chem. Phys.* **129** 234709
[24] Liu Z, Suenaga K, Harris P J F and Iijima S 2009 *Phys. Rev. Lett.* **102** 015501
[25] Snyman I and Beenakker C W J 2007 *Phys. Rev. B* **75** 045322
[26] Fiori G and Iannaccone G 2009 *IEEE Electron Dev. Lett.* **30** 1096
[27] Kuzmenko A B, Crassee I, Van Der Marel D, Blake P and Novoselov K S 2009 *Phys. Rev. B* **80** 165406
[28] Schulz C, Heinisch R L and Fehske H 2015 *Phys. Rev. B* **91** 045130
[29] Puls C P, Staley N E and Liu Y 2009 *Phys. Rev. B* **79** 235415
[30] Nilsson J, Castro Neto A H, Guinea F and Peres N M R 2007 *Phys. Rev. B* **76** 165416
[31] González J W, Santos H, Pacheco M, Chico L and Brey L 2010 *Phys. Rev. B* **81** 195406
[32] Koshino M, Nakanishi T and Ando T 2010 *Phys. Rev. B* **82** 205436
[33] Hasegawa Y and Kohmoto M 2012 *Phys. Rev. B* **85** 125430
[34] Tian J F, Jiang Y J, Childres I, Cao H L, Hu J P and Chen Y P 2013 *Phys. Rev. B* **88** 125410
[35] Zhang Y T, Jiang H, Sun Q F and Xie X C 2010 *Phys. Rev. B* **81** 165404
[36] Xu D W, Liu H W, Sacksteder V, Song J T, Jiang H, Sun Q F and Xie X C 2013 *J. Phys.: Condens. Matter* **25** 105303
[37] Avsar A, Vera-Marun I J, Tan J Y, Koon G K W, Watanabe K, Taniguchi T, Adam S and Özyilmaz B 2016 *NPG Asia Mater.* **8** e274
[38] Huard B, Sulpizio J A, Stander N, Todd K, Yang B and Goldhaber-Gordon D 2007 *Phys. Rev. Lett.* **98** 236803
[39] Abanin D A and Levitov L S 2007 *Science* **317** 641
[40] Özyilmaz B, Jarillo-Herrero P, Efetov D, Abanin D A, Levitov L S and Kim P 2007 *Phys. Rev. Lett.* **99** 166804
[41] Beenakker C W J, Akhmerov A R, Recher P and Tworzydlo J 2008 *Phys. Rev. B* **77** 075409
[42] Li J and Shen S Q 2008 *Phys. Rev. B* **78** 205308
[43] Balev O G and Vasko F T 2010 *J. Appl. Phys.* **107** 124312
[44] Zheng J M, Guo P, Ren Z Y, Jiang Z Y, Bai J T and Zhang Z Y 2012 *Appl. Phys. Lett.* **101** 083101
[45] Chung H C, Lin Y T, Lin S Y, Ho C H, Chang C P and Lin M F 2016 *Carbon* **109** 883
[46] González J W, Santos H, Prada E, Brey L and Chico L 2011 *Phys. Rev. B* **83** 205402
[47] Nakanishi T, Koshino M and Ando T 2010 *Phys. Rev. B* **82** 125428
[48] Cheng S G, Zhou J J, Jiang H and Sun Q F 2016 *New J. Phys.* **18** 103024
[49] Zhao F, Xu L and Zhang J 2016 *J. Phys.: Condens. Matter* **28** 185001
[50] Yan W, Li S Y, Yin L J, Qiao J B, Nie J C and He L 2016 *Phys. Rev. B* **93** 195408
[51] Lee D H and Joannopoulos J D 1981 *Phys. Rev. B* **23** 4997
[52] Sancho M P L, Sancho J M L and Rubio J 1984 *J. Phys. F: Met. Phys.* **14** 1205
[53] Sancho M P L, Sancho J M L and Rubio J 1985 *J. Phys. F: Met. Phys.* **15** 851
[54] An online program is available in the supplementary materials of reference, Sun Q F and Xie X C 2010 *Phys. Rev. Lett.* **104** 066805
[55] Guo H M, Feng S and Shen S Q 2011 *Phys. Rev. B* **83** 045114
[56] Guo H M 2010 *Phys. Rev. B* **82** 115122
[57] Zhang Y, Jiang Z, Small J P, Purewal M S, Tan Y W, Fazlollahi M, Chudow J D, Jaszczak J A, Stormer H L and Kim P 2006 *Phys. Rev. Lett.* **96** 136806
[58] Gusynin V P and Sharapov S G 2005 *Phys. Rev. Lett.* **95** 146801
[59] McCann E and Fal'ko V I 2006 *Phys. Rev. Lett.* **96** 086805
[60] Li J, Martin I, Büttiker M and Morpurgo A F 2011 *Nat. Phys.* **7** 38
[61] Chen J C, Yeung T C A and Sun Q F 2010 *Phys. Rev. B* **81** 245417
[62] Chen J C, Zhang H, Shen S Q and Sun Q F 2011 *J. Phys.: Condens. Matter* **23** 495301